# Oxygen Vacancy Formation and Reduction Properties of β-MnO$_2$ Grain Boundaries and the Potential for High Electrochemical Performance

James A. Dawson* and Isao Tanaka

Department of Materials Science and Engineering, Kyoto University, Sakyo, Kyoto 606-8501, Japan

ABSTRACT: In recent years, the nanostructuring of rutile (β-)MnO$_2$ has been shown to vastly improve its properties and performance in a number of technological applications. The contrast between the strong electrochemical properties of the nanostructured material and the bulk material that shows limited Li intercalation and electrochemical capacitance is not yet fully understood. In this work, we investigate the structure, stability and catalytic properties of four tilt grain boundaries in β-MnO$_2$ using interatomic potential methods. By considering the γ-surfaces of each of the grain boundaries, we are able to find the lowest energy configurations for each grain boundary

$$O_O^x + 2Mn_{Mn}^x \rightarrow V_O^{\bullet\bullet} + 2Mn_{Mn}^{/} + \frac{1}{2}O_{2(g)}$$

structure. For each grain boundary, we observe a significant decrease in the oxygen vacancy energies in and around the grain boundaries compared to bulk β-MnO$_2$ and also the bulk-like structures in the grain boundary cells. The reduction of Mn^{4+} to Mn^{3+} is also considered and again is shown to be preferable at the boundaries. These energies suggest a potentially higher catalytic activity at the grain boundaries of β-MnO$_2$. The results are also placed into context with recent calculations of β-MnO$_2$ surfaces to produce a more detailed understanding into this important phenomenon.

KEYWORDS: cathode material, grain boundaries, catalyst, lithium battery, supercapacitor
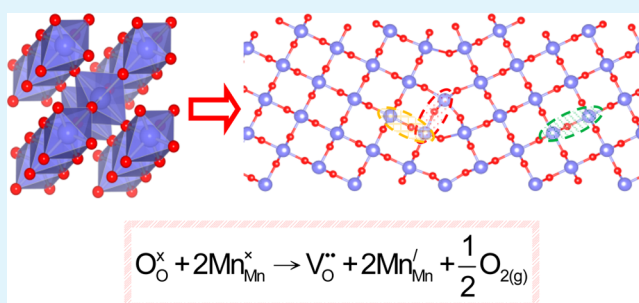
1. INTRODUCTION

The need for materials with a higher capacity and energy storage for various applications including hybrid electric vehicles and renewable energy sources is an ongoing issue in materials and energy science. Some major advantages of β-MnO$_2$ as an electrode material and catalyst are its easy preparation, low cost and low toxicity.[1] This is especially true when compared to conventional Co-containing battery materials like LiCoO$_2$[2] or Pt-based catalysts for oxygen reduction reactions (ORRs).[3] The search for safer, cheaper and more efficient energy storage materials has resulted in considerable research of manganese oxides.[4−7]

One of the most important and active research fields for β-MnO$_2$ is its application in Li-ion batteries. Early studies into bulk β-MnO$_2$ showed no significant Li-ion intercalation[6,8,9] as a possible result of the narrow tunnels present in the rutile structure.[10] However, recent work has shown that nano-composite and mesoporous β-MnO$_2$ samples show good Li-ion intercalation,[2,11,12] high capacities[6,11,13] of up to 320 mAh g^{-1} and good cycling stability.[6,14] Furthermore, ac impedance measurements have demonstrated increased Li diffusion in nanosized materials.[14,15] Despite the clear need for an understanding of why nanostructuring drastically improves many of the electrochemical properties of this material, it is only very recently that the interfaces of this material have been analyzed in any great detail. So far, the focus has been on surfaces and their impact on electrochemical properties.[2,14] In this work, we use computational techniques to produce the first

assessment of grain boundaries in this material and assess their potential influence on its electrochemical properties.

In addition to its use as an electrode material, MnO$_2$ is also well-known for its performance in numerous catalytic processes. Recent efforts have focused on its use in electro-chemical ORRs, which are essential in a variety of energy storage and conversion applications including metal−air batteries and fuel cells.[2,7,16] A prime example of this technology is the Li−O$_2$ battery, which is an alternative to conventional Li-ion batteries and could potentially significantly increase specific energy density.[2,17] However, it has been shown that these batteries are susceptible to overpotentials and rate limitations.[2,18] Fortunately, studies have suggested that the use of transition metals nanowires including rutile MnO$_2$ reduces overpotentials as well as improves cycling stability.[19−21] Although some studies have questioned the usefulness of such catalysts as a result of electrolyte decomposition,[22,23] it is clear that a good understanding of the role these materials have on ORRs is essential. Tompsett et al.[2] provide a good overview of the other catalytic applications of manganese oxides, which range from the oxidation of Cr^{3+} to Cr^{4+}[24,25] to reduction of NO$_x$.[26]

One other important major application of β-MnO$_2$ is as a supercapacitor. As with Li-ion batteries, bulk β-MnO$_2$ shows

limited applications for supercapacitors[27] with a capacitance of around only 9 F g^{-1}. However, again, nanostructuring of β-MnO$_2$ has been proven to significantly improve the electrochemical performance of the material. Nanostructuring of the material has been shown[28] to increase the capacitance to 294 F g^{-1}. In recent years, graphene and nanostructured MnO$_2$ composites have become a powerful combination in the search for low cost energy storage and conversion systems with high performance.[29−31] It is thought that the cause of this dramatic increase in capacitance is a result of the greater surface area exposure as a result of the nanostructuring.[2]

The impact of interfaces on such electrochemical processes is still not well-known and this is even more so for grain boundaries. It is also not clear what the concentration of grain boundaries is in these nanostructured β-MnO$_2$ samples. Although grain boundaries will play a more significant role in determining the properties of bulk samples, the grain boundary concentration in the more electrochemically active nano-structured samples will be significantly reduced. However, grain boundaries adjacent to the highly active surfaces in these samples are likely to be important in influencing the electrochemical properties. Given the importance of oxygen vacancy formation in these processes, it is essential that a study with the focus on grain boundaries is completed to complement previous surface and bulk studies.

Considering the amount of research focused on β-MnO$_2$ and its simple bulk structure, it could be expected that there is a good understanding of and considerable data available on the grain boundary structures of this material; unfortunately, this is not the case. This is true for both experimental and simulation studies. Works by Sayle et al.[13,32] and Maphanga et al.[33] focus on molecular dynamics simulations of the prediction of electrochemical properties for a variety of MnO$_2$ nanoparticles as well as amorphization and recrystallization of Li-ion insertion into MnO$_2$. Even in these studies, grain boundaries are only treated indirectly and are a result of the recrystallization process. Although data for rutile MnO$_2$ grain boundaries is very limited, there is both a wealth of computational[34−36] and experimental[37−39] information for rutile TiO$_2$. Although structural comparison with TiO$_2$ is far from ideal, the two materials have the same rutile structure, meaning it can still be a helpful tool for checking the validity of the calculated MnO$_2$ grain boundary structures.

Other than those mentioned previously, all computational studies of rutile MnO$_2$ have focused on the bulk and surface structures. Franchini et al.[40] used density functional theory (DFT) and hybrid DFT calculations to assess the structural, electronic, magnetic and thermodynamical properties of multiple bulk manganese oxides polymorphs. The relative strengths and weaknesses of each computational approach in calculating said properties were reported. One recent study[1] focuses on the lithiation of bulk β-MnO$_2$ using DFT and cluster expansion calculations. Electrochemical potentials of 3.47 to 2.77 eV are calculated for the lithiation process and Jahn−Teller distortion occurs as a result of mixed Mn valence states. This distortion is found to be responsible for asymmetric deformation during charge−discharge, which results in the irreversible capacity fading during cycling. DFT+U has also been used to study the phase stability of K-doped β-MnO$_2$.[41]

The simulation of β-MnO$_2$ surfaces has received considerable attention in recent times. The majority of these works used ab initio methods; however, one exception is the work of Maphanga et al.[42] where interatomic potentials are used to

study low index surfaces of β-MnO$_2$. Two studies by Oxford and Chaka[43,44] use the generalized gradient approximation (GGA) to also study low index surfaces. The surface energies of stoichiometric as well as heavily oxidized and reduced surfaces are calculated. Surface hydration is also considered. The effect of oxygen vacancies and hydrogen on the (110) surface of β-MnO$_2$ has also been assessed in a joint experimental−computational study.[7] This work shows how the catalytic activity of β-MnO$_2$ can be enhanced with only the introduction of oxygen deficiency. One weakness of the standard GGA is the poor reproduction of the electronic structure;[40] this has led authors to apply on-site Coulombic interactions in the form of the DFT+U calculations. Mellan et al.[45] used this approach for calculating lithium and oxygen adsorption at the (110) surface of β-MnO$_2$. Tompsett et al.[2,14] also used GGA+U to consider the importance of surface to bulk Li-ion migration as well as the structure of numerous β-MnO$_2$ surfaces and the effect oxygen vacancy formation has on the catalytic properties of these surfaces. They found that the formation energies of oxygen vacancies and Mn reduction were low compared to the bulk and other rutile structures which suggested high electrochemical performance of β-MnO$_2$ surfaces.

In this work, we use interatomic potential methods to analyze the stabilities and structures of a variety of tilt boundaries in β-MnO$_2$. We also predict the potential catalytic activity of these grain boundaries by calculating oxygen vacancy and reduction energies and comparing the results to values obtained for the bulk. We begin by describing the computational methods and our justification for using such methods. This is followed by details of the grain boundary construction and a discussion of their stabilities and structures. Finally, we discuss the calculated energies of oxygen vacancy formation and Mn4+ reduction and the consequences for catalytic activity.

2. COMPUTATIONAL METHODS

Although the use of ab initio methods is often preferred for calculations on systems with complex electronic and magnetic properties because of their high accuracy, interatomic potentials are chosen here because of their computational efficiency. When considering complex, low symmetry structures with supercells containing several hundred of atoms, it becomes exceptionally computationally time-consuming to test all the necessary configurations and to complete hundreds of calculations of oxygen vacancy formation or Mn reduction. Conversely, for interatomic potential methods, both the duration and quantity of the calculations is far more manageable. There are numerous examples of DFT calculations of grain boundaries in the literature; however they are usually confined to around 100 atoms[37] when multiple grain boundaries are considered or only one kind of boundary is simulated with a limited number of calculations on the obtained lowest energy structure.[46] As the results in this work will show, for most grain boundaries, 100 atoms is not enough to achieve convergence, as the distance between the two equivalent grain boundaries is not sufficient, which can result in unrealistic interactions between the boundaries.

The interionic interactions in this work are simulated using the Born model for ionic solids. In this model, ions are treated as charged spheres where the short-range forces are accounted for by the interatomic potentials and the long-range ionic interactions are treated using Coulombic terms. The methods discussed in this section are very well established and comprehensive reviews are available elsewhere.[47] For this work, we use the proven potential model of Maphanga et al.[33,42] Often, interatomic potential models are not adequate in simulating highly distorted systems with under-coordinated atoms. However, this potential model was originally fitted for the purpose of simulating amorphous configurations and not only reproduces the rutile, ramsdellite and pyrolusite phases of MnO$_2$, but also correctly

predicts their energetic stability.[33,42] This model has also been successfully used for a number of other studies of β-MnO$_2$[13,32] and has recently been applied to find the lowest energy surface structures of the material.[2] The interatomic potentials used to model MnO$_2$ in this work take the Buckingham form:

$$V_{ij}(r) = \sum_{i \neq j}^{n} A \exp(-r_{ij}/\rho) - \frac{C}{r_{ij}^{6}} \tag{1}$$

where the symbols have their usual meanings. The charges of the Mn and O ions are represented by a rigid ion model with partial charges. The parameters for all the interatomic potentials used in this work are given in Table 1. A cutoff of 12 Å was applied to all of the potentials.

Table 1. Mn−O and O−O Buckingham Potential Parameters used for β-MnO$_2$

interaction	A (eV)	ρ (eV)	C (eV Å^{-6})
Mn$^{2.2+}$−O$^{1.1-}$ (Mn^{4+})	15538.20	0.195	22.00
Mn$^{1.65+}$−O$^{1.1-}$ (Mn^{3+})	18645.84	0.195	22.00
Mn$^{2.2+}$−Mn$^{2.2+}$	23530.50	0.156	16.00
Mn$^{2.2+}$−Mn$^{1.65+}$	28707.21	0.156	16.00
Mn$^{1.65+}$−Mn$^{1.65+}$	33883.92	0.156	16.00
O$^{1.1-}$−O$^{1.1-}$	11782.76	0.234	30.22

The β-MnO$_2$ structure is presented in Figure 1 and the calculated and experimental lattice parameters are displayed in Table 2. The
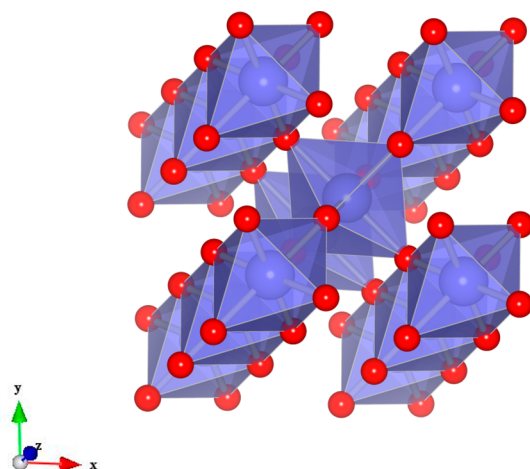
Figure 1. Crystal structure of β-MnO$_2$. The blue spheres at the center of the octahedra are manganese ions and the red spheres at the edge of the octahedra are oxygen ions. The narrow tunnel structure can be observed along the z-axis.

model reproduces the lattice parameters of the bulk β-MnO$_2$ structure to within 2% of experiment.

Point defects and dopant ions are simulated at the infinitely dilute limit using the Mott−Littleton method.[49] The area surrounding the defect is divided into an inner and outer region. In the inner region atomic interactions are calculated explicitly, whereas in the outer region (where the interactions are weaker) they are approximated using a dielectric continuum method:

Table 2. Experimental and Calculated Lattice Parameters for β-MnO$_2$

	a (Å)	b (Å)	c (Å)
calculated	4.401	4.401	2.925
experiment[48]	4.398	4.398	2.873

$$E = E_1(x) + E_{12}(x, \eta) + E_2(\eta) \tag{2}$$

where E_1 and E_2 are the energies of the inner and outer regions, respectively, and E_{12} is the energy of the interactions between them. Atomic displacements are denoted by x and η for the inner and outer regions, respectively. All the calculations in this work were completed using the General Utility Lattice Program (GULP).[50]

3. RESULTS AND DISCUSSION

3.1. Grain Boundary Structures. The importance of interfaces in β-MnO$_2$ on the materials electrochemical properties and therefore application in various energy technologies has been made clear. Through the use of classical simulations, we can predict the preferred grain boundary structures and calculate their energetic stabilities. We consider four tilt grain boundaries in this study: Σ 5(210)/[001], Σ 5(310)/[001], Σ 13(510)/[001] and Σ 17(530)/[001]. These common grain boundaries were chosen, as they provide a wide variety of grain boundary angles and physical dimensions as well as being common to the rutile structure. The starting grain boundary configurations are formed using coincidence site lattice (CSL) theory where two individual grains are tilted by a given angle until there surface planes coincide. The 240 atom unoptimized starting configurations are displayed in Figure 2. It is essential all grain boundary structures are longest in the z direction in order to minimize the interactions between the equivalent grain boundaries at the center and edges of the supercells.

An issue with simulating grain boundary configurations is that there are often ions with the same charge in close proximity at the boundary. This leads to increased Coulombic repulsion, causing unstable grain boundaries with high energies. A solution to this problem is to introduce vacancies across the grain boundary and half the atom density. This approach has been successfully used for YSZ grain boundaries.[51,52] However, this method is usually used when ions at the boundary are in very close proximity and when γ-surface exploration does not produce sufficiently low enough grain boundary energies. This is not the case for our chosen rutile MnO$_2$ grain boundaries. Therefore, we address the issue by the common approach of exploring the γ-surface of the grain boundaries. Using rigid body translations, one grain can be displaced with respect to the other in various three-dimensional translation states. This method is crucial in finding the global minimum and works by calculating the grain boundary energy at each translation. The grain boundary energy is calculated by

$$\sigma_{GB} = \frac{E_{GB} - E_{bulk}}{2A} \tag{3}$$

where E_{GB} and E_{bulk} are the energies of the grain boundary and the bulk supercell, respectively, and A is the area of the interface. The area of the interface is doubled to account for the presence of the two equivalent grain boundaries in the supercell. The energy was calculated as a function of translation states with increments of about 0.01 nm. This approach has been used for atomistic simulations of numerous grain boundaries in many different materials.[39,53−55] Table 3 shows the lowest calculated grain boundary energy and cell dimensions for each grain boundary. Our grain boundary energies were obtained from supercells with 240−360 atoms. Convergence with grain boundary separation was tested and achieved using a selection of supercells with fewer atoms and smaller z cell dimensions.
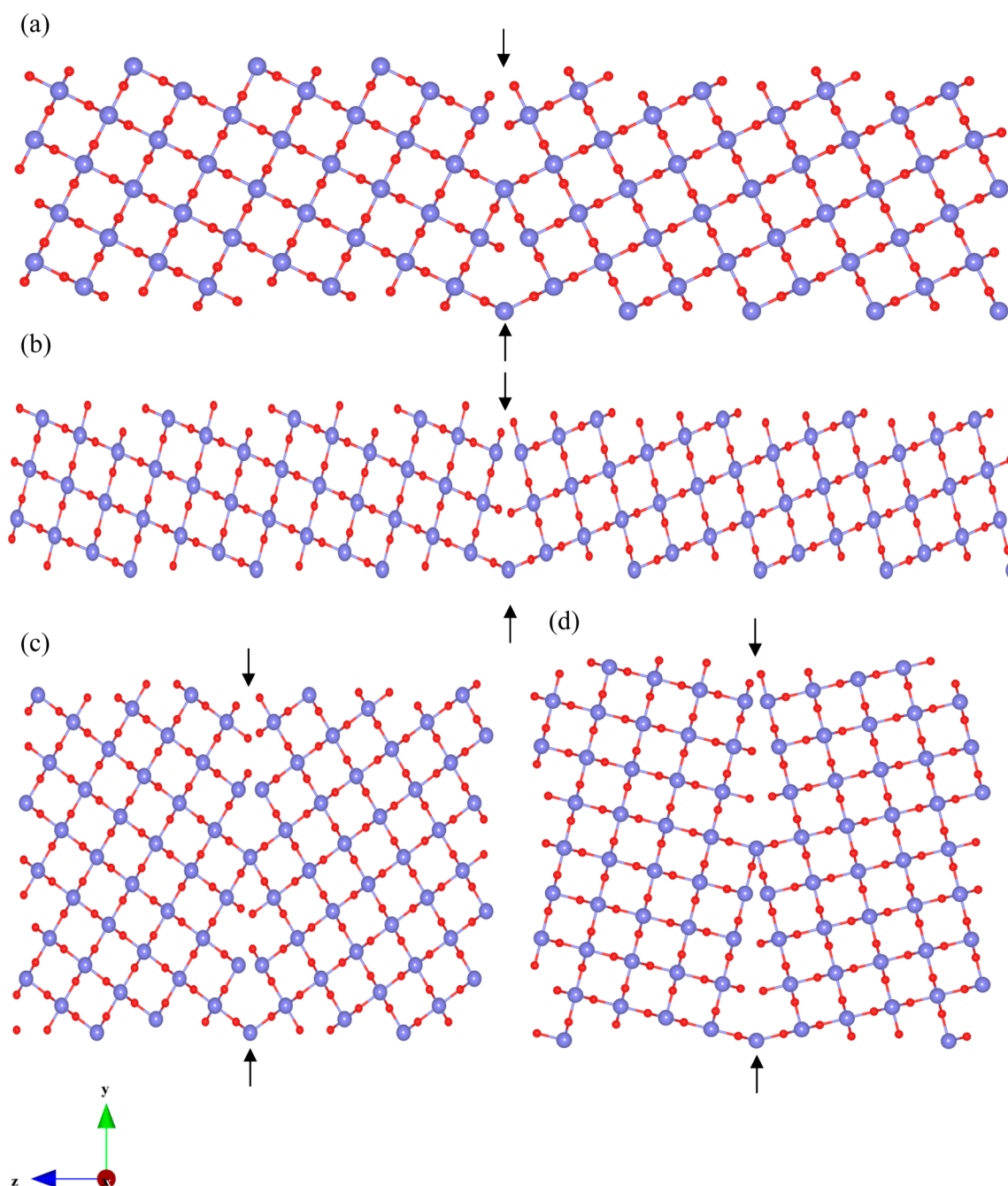
Figure 2. Initial structures of the (a) Σ 5(210)/[001], (b) Σ 5(310)/[001], (c) Σ 13(510)/[001] and (d) Σ 17(530)/[001] β-MnO$_2$ grain boundaries. The grain boundaries are located at the center and edges of the supercells. Large blue spheres are manganese and small red spheres are oxygen.

It is clear from Table 3 that there is a significant spread in the energies for the different grain boundary energies. The Σ 5(210)/[001] grain boundary is the most stable, most likely as a result of the fact that the interatomic distances between ions of the same type at the boundary are larger than for the other grain boundaries. This is supported by the high grain boundary energy calculated for Σ 17(530)/[001]. In this grain boundary, some of the interatomic distances are far shorter than the typical 1.88−1.91 Å Mn−O bonds in bulk β-MnO$_2$. Energies for the Σ 5(210)/[001] and Σ 5(310)/[001] grain boundaries have been previously calculated for rutile TiO$_2$ using computational methods.[37,38,56] In DFT calculations by Körner and Elsässer,[37] Σ 5(210)/[001] (1.92 J m^{-2}) is also predicted to be the more stable than Σ 5(310)/[001] (2.84 J m^{-2}). Dawson et al.[38] also used DFT to calculate an energy of 1.72 J m^{-2} for Σ 5(210)/[001], which is marginally higher than the value of 1.70 J m^{-2} calculated using interatomic potential methods.[56] All of these values are higher than our value of 1.53 J m^{-2}. This is likely to be a result of insufficient cell sizes used in the previous calculations and the fact that two different rutile structured materials will not have the exact same grain boundary energies. It is also possible that rigid body translations were not considered in some of these works. It is noteworthy that our results show that convergence is not always proportional to grain boundary separation.

Table 3. β-MnO₂ Grain Boundary Energies, Physical Parameters and the Number of Atoms Required for Convergence

grain boundary	energy (J m⁻²)	cell dimensions (x, y, z) (Å)	grain boundary separation (Å)	atom number convergence
Σ 5(210)/[001]	1.53	2.93, 13.92, 83.50	41.75	360
Σ 5(310)/[001]	2.96	2.93, 9.84, 78.73	39.37	240
Σ 13(510)/[001]	2.53	2.93, 22.44, 51.79	25.90	360
Σ 17(530)/[001]	3.12	2.93, 25.66, 37.74	18.87	300

The optimized, lowest energy grain boundary structures demonstrate the dramatic impact that rigid-body translations can have on the final structures. For example, for the Σ 17(530)/[001] boundary, rigid-body translations reduced the energy by almost 25%, which clearly illustrates the importance of thoroughly exploring the γ-surface. Figure 3 shows the Σ
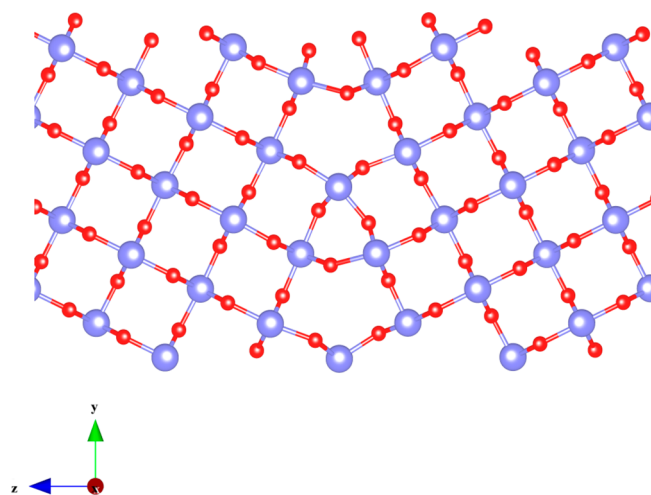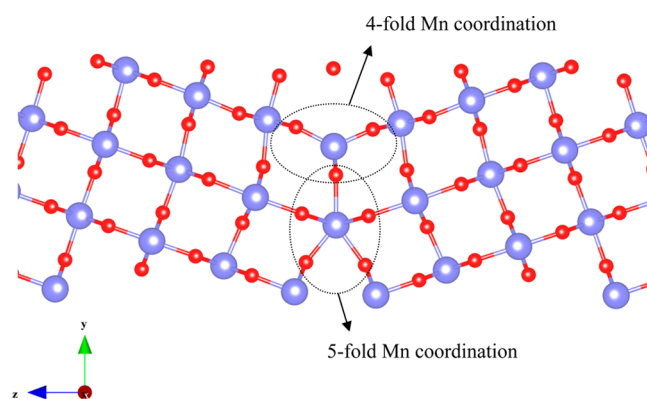

Figure 3. Optimized structure for the Σ 5(210)/[001] β-MnO₂ grain boundary.

5(210)/[001] grain boundary after rigid-body translations and optimization. Comparison of Figures 2 and 3 shows that the translations applied to this grain boundary to achieve the lowest energy structure are subtle. This to be expected given that the interatomic distances at the grain boundary of the initial structure are similar to that of the bulk and as a result this boundary has by far the lowest energy. While there is some distortion of the octahedra at the grain boundary, the 6-fold coordination of the Mn ions and the 3-fold coordination of the oxygen ions are mostly preserved. However, overcoordination does occur for a few select at the grain boundary. Our structure is in good agreement with previous works[37,39] that showed no significant rigid-body contraction or expansion.

To further assess the validity of the Σ 5(210)/[001] β-MnO₂ grain boundary, as well as the accuracy of the potential model, we completed further calculations using DFT. Using the VASP code[57] with PAW potentials and the GGA of Perdew, Burke and Ernzerhof,[58] we simulated the lowest energy structure found using potentials as well as the starting grain boundary configuration and other selected low energy structures. For a 180 atom supercell, we calculated a grain boundary energy of

1.45 J m⁻², in excellent agreement with the value calculated from the interatomic potentials (1.53 J m⁻²). This value was also lower than the respective values for the starting configuration and the other low energy structures. The DFT calculated structure was also almost identical to the structure calculated from potentials. We can therefore assume that our chosen potential model is capable of accurately modeling these defective structures.
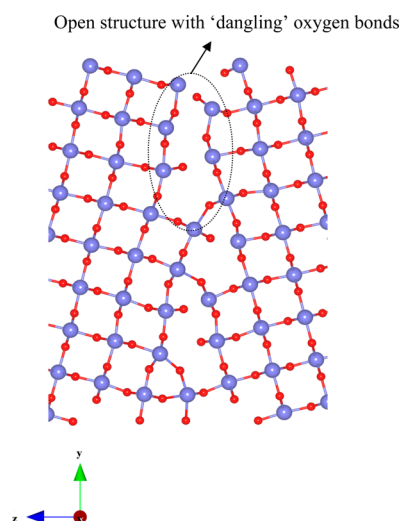
The optimized Σ 5(310)/[001] grain boundary is given in Figure 4. For this grain boundary, the distortion is significantly

Figure 4. Optimized structure for the Σ 5(310)/[001] β-MnO₂ grain boundary.

stronger. The Mn ions at the center of the grain boundary have reduced coordination (5-fold or 4-fold), as do a number of the oxygen ions (2-fold). This structure exhibits a large translation in the x direction, which causes the unusual 5-fold coordination of the Mn ion at the center of the grain boundary. A number of the bonds around the central Mn ions are longer than the usual equilibrium distances which suggests an unfavorable grain boundary structure and therefore high grain boundary energy.

The Σ 13(510)/[001] and Σ 17(530)/[001] grain boundaries are presented in Figures 5 and 6, respectively. Both grain boundaries show significant under coordination for ions at the grain boundary. While some of the Mn ions in the Σ 13(510)/[001] boundary form a kind of bridging structure where two oxygen ions are shared between two Mn ions, others
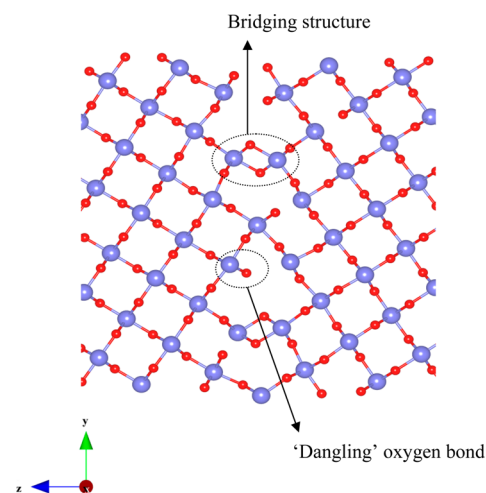
Figure 5. Optimized structure for the Σ 13(510)/[001] β-MnO₂ grain boundary.

Open structure with 'dangling' oxygen bonds

Figure 6. Optimized structure for the Σ 17(530)/[001] β-MnO$_2$ grain boundary.

Table 4. Average Oxygen Vacancy Energies for β-MnO$_2$ Grain Boundaries

grain boundary	R1 oxygen vacancy energy (eV)	R2 oxygen vacancy energy (eV)	R3 oxygen vacancy energy (eV)
Σ 5(210)/[001]	8.58	9.38	9.66
Σ 5(310)/[001]	7.03	7.33	9.68
Σ 13(510)/[001]	7.66	8.60	9.70
Σ 17(530)/[001]	7.13	7.15	9.65

GB adjacent layers (R2)   GB core (R1)   Bulk-like region (R3)

Figure 7. Illustration of the three different supercell regions used for the oxygen vacancy and reduction cluster calculations.

are left with 4- or 5-fold coordination. There are also a large number of "dangling" oxygen bonds present at the Σ 13(510)/ [001] grain boundary. For the Σ 17(530)/[001] grain boundary, there are even more undercoordinated oxygen ions and there is also a larger number of open structures compared to the other grain boundaries. It has been noted previously that such open structures and undercoordinated oxygen ions are likely to be good adsorption sites for hydrogen (and other dopant ions) when rutile MnO$_2$ is used as a supercapacitor electrode.[2] These two reasons are also likely responsible for why this grain boundary is the least stable of the four tested.
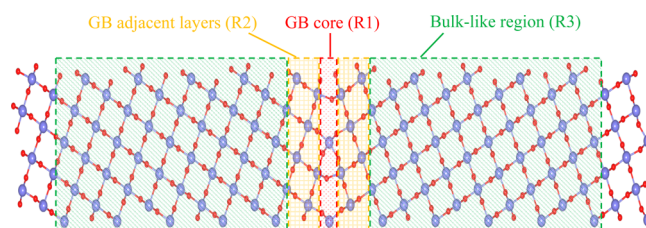
3.2. Oxygen Vacancy and Reduction Cluster Formation. The formation of oxygen vacancies and the reduction of Mn^{4+} to Mn^{3+} are essential for the catalytic applications of MnO$_2$. Numerous studies have illustrated the importance of these defects for catalyzed reactions like the ORR[59−61] and the enhancement they can have on catalytic performance.[2,7] Previous work on the energetics of oxygen vacancy formation is somewhat limited. However, one exception is the work of Tompsett et al.[2] where DFT+U was used to calculate oxygen vacancy formation energies for a number of β-MnO$_2$ surfaces. Oxygen vacancy energies for each surface tested were all lower than the value obtained for the bulk material. Furthermore, the calculated values were lower than those for rutile TiO$_2$ surfaces. It is proposed that these favorable oxygen vacancy defects may play a signifcant role in the favorable catalytic performance of β-MnO$_2$. The results presented here form the first ever assessment of the energetics of reduction and oxygen vacancy formation in β-MnO$_2$ grain boundaries.

The calculated average oxygen vacancy energies for three different grain boundary supercell regions are presented in Table 4. These three sections are defined for the Σ 5(210)/ [001] grain boundary in Figure 7. By calculating the energies at the grain boundary core region (R1), the adjacent layers of the grain boundary (R2) and the bulk-like region (R3) in the supercell, we can easily decide which area favors oxygen vacancies and therefore assess the potential contribution to the catalytic activity.

There are two main points of discussion for the oxygen vacancy calculations. First, for all the grain boundaries structures, the vacancy energies are lower at the boundary and the surrounding area compared to the bulk-like region and

the value calculated for standard bulk rutile MnO$_2$ (9.69 eV). This is the same as what was observed for oxygen vacancies at β-MnO$_2$ surfaces.[2] This result suggests that it may not only be the surfaces that contribute to this materials excellent catalytic performance, but also the grain boundaries. It is clear that it is the interfaces of rutile MnO$_2$ and not the bulk structure that determine its catalytic properties. Second, the oxygen vacancy energies at the interface are highest for the most energetically stable grain boundary, Σ 5(210)/[001]. This is to be expected given that the optimized structure of this grain boundary is the most simple and the oxygen ions at the boundary maintain their coordination number. Direct comparison of the values calculated here and the ones calculated by Tompsett et al.[2] is difficult because of the different methodologies used; however, the similarity in the trends is absolutely valid.

In addition to oxygen vacancy energies, the calculation of the energy of reduction is important in assessing the impact of the grain boundary structures on the performance of the material. In this work, we calculate the energy of reduction clusters, which consist of an oxygen vacancy and two reduced Mn^{3+} ions. The formation of this cluster is expressed by

$$O_O^x + 2Mn_{Mn}^x \rightarrow V_O^{\bullet\bullet} + 2Mn_{Mn}' + \frac{1}{2}O_{2(g)} \qquad (4)$$
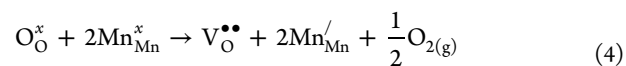
The substitution of a Mn^{3+} ion at a Mn^{4+} site was calculated using the Mn^{3+} interatomic potentials from the Maphanga et al.[33,42] potential set. Example reduction cluster configurations for each region are given in Figure 8. For each oxygen ion, the two closest neighboring Mn ions were chosen to form the three defect cluster. By calculating all the defects in one cluster, we are able to take into account the binding energy between the oppositely charged defects. The energies of the reduction clusters in each of the three grain boundary cell environments are displayed in Table 5.

The results for the reduction cluster energies exhibit the same main trend as the oxygen vacancy results. Again, the values at the core and adjacent layers are significantly lower than the bulk values; however, it is interesting that for two of the grain boundaries, the energy at the area surrounding the grain boundary is lower than at the core. This is not the case for the oxygen vacancies. The reduction energy for the bulk cell was calculated to be 35.17 eV. This is significantly higher than
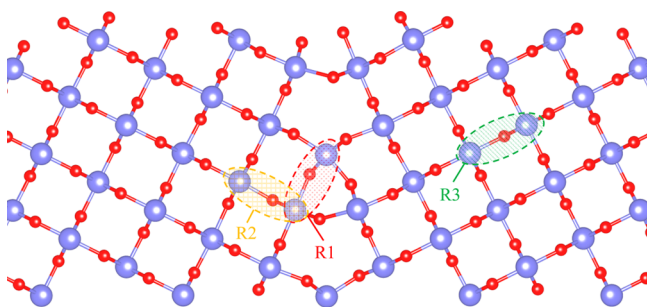
Figure 8. Example reduction clusters for each of the three supercell regions.

Table 5. Average Reduction Cluster Energies for β-MnO₂ Grain Boundaries

grain boundary	R1 reduction cluster energy (eV)	R2 reduction cluster energy (eV)	R3 reduction cluster energy (eV)
Σ 5(210)/[001]	33.22	33.96	34.47
Σ 5(310)/[001]	32.39	32.01	34.50
Σ 13(510)/[001]	32.47	33.57	34.56
Σ 17(530)/[001]	33.77	32.04	34.41

the calculated values for the bulk-like region and the difference is also larger than what is observed for the oxygen vacancy energies calculated for the bulk and bulk-like regions. This suggests that the grain boundaries can influence the reduction energy of Mn^{4+} ions that are several layers away. For all the reduction clusters, the binding energies are strong and negative, which suggests that oxygen vacancies are stable when in these defect clusters. Currently, it is unclear how much these interfaces contribute to the catalytic properties of nano-structured β-MnO₂, especially when compared to the surface activity. However, it is doubtless that these new results warrant further inverstigation. In subsequent publications, we will attempt to further assess the contribution of the grain boundaries to the electrical properties of this material and also how the results compare to the grain boundaries of other rutile structured materials like TiO_2 and RuO_2.

4. CONCLUSIONS

In this study, we have used interatomic potential methods to investigate the structures and stabilities of β-MnO₂ grain boundaries and assess their impact on the catalytic properties of this technologically important material. We have considered four different grain boundaries and, by exploring their γ-surfaces, we found the lowest energy configurations for each structure. The Σ 5(210)/[001] grain boundary was found to be the most stable with a grain boundary energy of 1.53 J m⁻². Although the other three grain boundaries show signifcant undercoordination and as a result higher grain boundaries, the oxygen and manganese ions at the Σ 5(210)/[001] grain boundary remain fully coordinated. By calculating the average oxygen vacancy and reduction cluster energies at three different environments in the grain boundary supercells, we were able to assess the favored regions for vacancy formation and Mn ion reduction. Both the oxygen vacancy and reduction energies were lower at the grain boundary cores and surrounding areas. This is similar to what has been previously ascertained for β-MnO₂ surfaces. It is likely that such low energies contribute to the good catalytic properties of this material; however, it is not yet known how significant this contribution is for nano-

structured β-MnO₂, especially when compared to the high surface activity.

■ AUTHOR INFORMATION

Corresponding Author
*J. A. Dawson. E-mail: dawson.jamesalexander.2w@kyoto-u.ac.jp. Tel: +81-75-753-5435.
Notes
The authors declare no competing financial interest.

■ ACKNOWLEDGMENTS

■ REFERENCES

(1) Wang, D.; Liu, L.-M.; Zhao, S.-J.; Li, B.-H.; Liu, H.; Lang, X.-F. β-MnO₂ as a Cathode Material for Lithium Ion Batteries from First Principles Calculations. *Phys. Chem. Chem. Phys.* **2013**, *15*, 9075–9083.
(2) Tompsett, D. A.; Parker, S. C.; Islam, M. S. Rutile (β-)MnO₂ Surfaces and Vacancy Formation for High Electrochemical and Catalytic Performance. *J. Am. Chem. Soc.* **2014**, *136*, 1418–1426.
(3) Kloke, A.; von Stetten, F.; Zengerle, R.; Kerzenmacher, S. Strategies for the Fabrication of Porous Platinum Electrodes. *Adv. Mater.* **2011**, *23*, 4976–5008.
(4) Armstrong, A. R.; Bruce, P. G. Synthesis of Layered LiMnO₂ as an Electrode for Rechargeable Lithium Batteries. *Nature* **1996**, *381*, 499–500.
(5) Armstrong, A. R.; Holzapfel, M.; Novák, P.; Johnson, C. S.; Kang, S.-H.; Thackeray, M. M.; Bruce, P. G. Demonstrating Oxygen Loss and Associated Structural Reorganization in the Lithium Battery Cathode Li[Ni₀.₂Li₀.₂Mn₀.₆]O₂. *J. Am. Chem. Soc.* **2006**, *128*, 8694–8698.
(6) Jiao, F.; Bruce, P. G. Mesoporous Crystalline β-MnO₂—A Reversible Positive Electrode for Rechargeable Lithium Batteries. *Adv. Mater.* **2007**, *19*, 657–660.
(7) Cheng, F.; Zhang, T.; Zhang, Y.; Du, J.; Han, X.; Chen, J. Enhancing Electrocatalytic Oxygen Reduction on MnO₂ with Vacancies. *Angew. Chem., Int. Ed.* **2013**, *52*, 2474–2477.
(8) Thackeray, M. M.; David, W. I. F.; Bruce, P. G.; Goodenough, J. B. Lithium Insertion into Manganese Spinels. *Mater. Res. Bull.* **1983**, *18*, 461–472.
(9) Thackeray, M. M.; Johnson, C. S.; Vaughey, J. T.; Li, N.; Hackney, S. A. Advances in Manganese-Oxide "Composite" Electrodes for Lithium-Ion Batteries. *J. Mater. Chem.* **2005**, *15*, 2257–2267.
(10) Turner, S.; Buseck, P. R. Todorokites: A New Family of Naturally Occurring Manganese Oxides. *Science* **1981**, *212*, 1024–1027.
(11) Luo, J.-Y.; Zhang, J.-J.; Xia, Y.-Y. Highly Electrochemical Reaction of Lithium in the Ordered Mesoporosus β-MnO₂. *Chem. Mater.* **2006**, *18*, 5618–5623.
(12) Cheng, F.; Zhao, J.; Song, W.; Li, C.; Ma, H.; Chen, J.; Shen, P. Facile Controlled Synthesis of MnO₂ Nanostructures of Novel Shapes and Their Application in Batteries. *Inorg. Chem.* **2006**, *45*, 2038–2044.
(13) Sayle, T. X. T.; Maphanga, R. R.; Ngoepe, P. E.; Sayle, D. C. Predicting the Electrochemical Properties of MnO₂ Nanomaterials Used in Rechargeable Li Batteries: Simulating Nanostructure at the Atomistic Level. *J. Am. Chem. Soc.* **2009**, *131*, 6161–6173.
(14) Tompsett, D. A.; Parker, S. C.; Bruce, P. G.; Islam, M. S. Nanostructuring of β-MnO₂: The Important Role of Surface to Bulk Ion Migration. *Chem. Mater.* **2013**, *25*, 536–541.
(15) Bach, S.; Pereira-Ramos, J. P.; Willmann, P. A Kinetic Study of Electrochemical Lithium Insertion in Nanosized Rutile β-MnO₂ by Impedance Spectroscopy. *Electrochim. Acta* **2011**, *56*, 10016–10022.

(16) Kinoshita, K. *Electrochemical oxygen technology*; Wiley: New York, 1992.

(17) Bruce, P. G.; Freunberger, S. A.; Hardwick, L. J.; Tarascon, J.-M. Li-O₂ and Li-S Batteries with High Energy Storage. *Nat. Mater.* **2012**, *11*, 19−29.

(18) Ogasawara, T.; Débart, A.; Holzapfel, M.; Novák, P.; Bruce, P. G. Rechargeable Li₂O₂ Electrode for Lithium Batteries. *J. Am. Chem. Soc.* **2006**, *128*, 1390−1393.

(19) Lu, Y. C.; Xu, Z.; Gasteiger, H. A.; Chen, S.; Hamad-Schifferli, K.; Shao-Horn, Y. Platinum−Gold Nanoparticles: A Highly Active Bifunctional Electrocatalyst for Rechargeable Lithium−Air Batteries. *J. Am. Chem. Soc.* **2010**, *132*, 12170−12171.

(20) McCloskey, B. D.; Scheffler, R.; Speidel, A.; Bethune, D. S.; Shelby, R. M.; Luntz, A. C. On the Efficacy of Electrocatalysis in Nonaqueous Li−O₂ Batteries. *J. Am. Chem. Soc.* **2011**, *133*, 18038−18041.

(21) Thapa, A. K.; Hidaka, Y.; Hagiwara, H.; Ida, S.; Ishihara, T. Mesoporous β-MnO₂ Air Electrode Modified with Pd for Rechargeability in Lithium-Air Battery. *J. Electrochem. Soc.* **2011**, *158*, A1483−A1489.

(22) Freunberger, S. A.; Chen, Y.; Peng, Z.; Griffin, J. M.; Hardwick, L. J.; Bardé, F.; Novák, P.; Bruce, P. G. Reactions in the Rechargeable Lithium−O₂ Battery with Alkyl Carbonate Electrolytes. *J. Am. Chem. Soc.* **2011**, *133*, 8040−8047.

(23) Xiao, J.; Hu, J.; Wang, D.; Hu, D.; Xu, W.; Graff, G. L.; Nie, Z.; Liu, J.; Zhang, J. G. Investigation of the Rechargeability of Li−O₂ Batteries in Non-aqueous Electrolyte. *J. Power Sources* **2011**, *196*, 5674−5678.

(24) Eary, L. E.; Rai, D. Kinetics of Chromium(III) Oxidation to Chromium(VI) by Reaction with Manganese Dioxide. *Environ. Sci. Technol.* **1987**, *21*, 1187−1193.

(25) Weaver, R. M.; Hochella, M. F.; Ilton, E. S. Dynamic Processes Occurring at the Cr(aq)³⁺−Manganite Interface: Simultaneous Adsorption, Microprecipitation, Oxidation/Reduction and Dissolution. *Geochim. Cosmochim. Acta* **2002**, *66*, 4119−4132.

(26) Busca, G.; Lietti, L.; Ramis, G.; Berti, F. Chemical and Mechanistic Aspects of the Selective Catalytic Reduction of NOₓ by Ammonia Over Oxide Catalysts: A Review. *Appl. Catal. B: Environ.* **1998**, *18*, 1−36.

(27) Devaraj, S.; Munichandraiah, N. Effect of Crystallographic Structure of MnO₂ on Its Electrochemical Capacitance Properties. *J. Phys. Chem. C* **2008**, *112*, 4406−4417.

(28) Zang, J.; Li, X. In Situ Synthesis of Ultrafine β-MnO₂/Polypyrrole Nanorod Composites for High-Performance Supercapacitors. *J. Mater. Chem.* **2011**, *21*, 10965−10969.

(29) Chen, S.; Zhu, J.; Wu, X.; Han, Q.; Wang, X. Graphene Oxide−MnO₂ Nanocomposites for Supercapacitors. *ACS Nano* **2010**, *4*, 2822−2830.

(30) He, Y.; Chen, W.; Li, X.; Zhang, Z.; Fu, J.; Zhao, C.; Xie, E. Freestanding Three-Dimensional Graphene/MnO₂ Composite Networks as Ultralight and Flexible Supercapacitor Electrodes. *ACS Nano* **2012**, *7*, 174−182.

(31) Xie, X.; Zhang, C.; Wu, M.-B.; Tao, Y.; Lv, W.; Yang, Q.-H. Porous MnO₂ for Use in a High Performance Supercapacitor: Replication of a 3D Graphene Network as a Reactive Template. *Chem. Commun.* **2013**, *49*, 11092−11094.

(32) Sayle, T. X. T.; Catlow, C. R. A.; Maphanga, R. R.; Ngoepe, P. E.; Sayle, D. C. Generating MnO₂ Nanoparticles Using Simulated Amorphization and Recrystallization. *J. Am. Chem. Soc.* **2005**, *127*, 12828−12837.

(33) Maphanga, R. R.; Sayle, D. C.; Sayle, T. X. T.; Ngoepe, P. E. Amorphization and Recrystallization Study of Lithium Insertion into Manganese Dioxide. *Phys. Chem. Chem. Phys.* **2011**, *13*, 1307−1313.

(34) Dahmen, U.; Paciornik, S.; Solorzano, I. G.; Vandersande, J. B. HREM Analysis of Structure and Defects in a Σ5 (210) Grain Boundary in Rutile. *Interface Sci.* **1994**, *2*, 125−136.

(35) Nowotny, J.; Bak, T.; Burg, T.; Nowotny, M. K.; Sheppard, L. R. Effect of Grain Boundaries on Semiconducting Properties of TiO₂ at Elevated Temperatures. *J. Phys. Chem. C* **2007**, *111*, 9769−9778.

(36) Blas, P. U.; Xian-Ming, B. Defects in Rutile and Anatase Polymorphs of TiO₂: Kinetics and Thermodynamics Near Grain Boundaries. *J. Phys.: Condens. Mater.* **2011**, *23*, 435004.

(37) Körner, W.; Elsässer, C. Density Functional Theory Study of Dopants in Polycrystalline TiO₂. *Phys. Rev. B* **2011**, *83*, 205315.

(38) Dawson, I.; Bristowe, P. D.; Lee, M. H.; Payne, M. C.; Segall, M. D.; White, J. A. First-Principles Study of a Tilt Grain Boundary in Rutile. *Phys. Rev. B* **1996**, *54*, 13727−13733.

(39) Sinnott, S. B.; Wood, R. F.; Pennycook, S. J. Ab Initio Calculations of Rigid-Body Displacements at the Σ5 (210) Tilt Grain Boundary in TiO₂. *Phys. Rev. B* **2000**, *61*, 15645−15648.

(40) Franchini, C.; Podloucky, R.; Paier, J.; Marsman, M.; Kresse, G. Ground-State Properties of Multivalent Manganese Oxides: Density Functional and Hybrid Density Functional Calculations. *Phys. Rev. B* **2007**, *75*, 195128.

(41) Cockayne, E.; Li, L. First-Principles Studies of the Atomic, Electronic, and Magnetic Structure of α-MnO₂ (Cryptomelane). *Chem. Phys. Lett.* **2012**, *544*, 53−58.

(42) Maphanga, R. R.; Parker, S. C.; Ngoepe, P. E. Atomistic Simulation of the Surface Structure of Electrolytic Manganese Dioxide. *Surf. Sci.* **2009**, *603*, 3184.

(43) Oxford, G. A. E.; Chaka, A. M. First-Principles Calculations of Clean, Oxidized, and Reduced β-MnO₂ Surfaces. *J. Phys. Chem. C* **2011**, *115*, 16992−17008.

(44) Oxford, G. A. E.; Chaka, A. M. Structure and Stability of Hydrated β-MnO₂ Surfaces. *J. Phys. Chem. C* **2012**, *116*, 11589−11605.

(45) Mellan, T. A.; Maenetja, K. P.; Ngoepe, P. E.; Woodley, S. M.; Catlow, C. R. A.; Grau-Crespo, R. Lithium and Oxygen Adsorption at the β-MnO₂ (110) Surface. *J. Mater. Chem. A* **2013**, *1*, 14879−14887.

(46) Moriwake, H.; Kuwabara, A.; Fisher, C. A. J.; Huang, R.; Hitosugi, T.; Ikuhara, Y. H.; Oki, H.; Ikuhara, Y. First-Principles Calculations of Lithium-Ion Migration at a Coherent Grain Boundary in a Cathode Material, LiCoO₂. *Adv. Mater.* **2013**, *25*, 618−622.

(47) Harding, J. H. Computer Simulation of Defects in Ionic Solids. *Rep. Prog. Phys.* **1990**, *53*, 1403.

(48) Baur, W. Rutile-Type Compounds. V. Refinement of MnO₂ and MgF₂. *Acta Crystallogr. B* **1976**, *32*, 2200−2204.

(49) Mott, N. F.; Littleton, M. J. Conduction in Polar Crystals. I. Electrolytic Conduction in Solid Salts. *Trans. Faraday Soc.* **1938**, *34*, 485−499.

(50) Gale, J. D.; Rohl, A. L. The General Utility Lattice Program (GULP). *Mol. Simul.* **2003**, *29*, 291−341.

(51) Yoshiya, M.; Oyama, T. Impurity and Vacancy Segregation at Symmetric Tilt Grain Boundaries in Y₂O₃-Doped ZrO₂. *J. Mater. Sci.* **2011**, *46*, 4176−4190.

(52) Dawson, J. A.; Tanaka, I. Significant Reduction in Hydration Energy for Yttria Stabilized Zirconia Grain Boundaries and the Consequences for Proton Conduction. *Langmuir* **2014**, *30*, 10456−10464.

(53) Oba, F.; Ohta, H.; Sato, Y.; Hosono, H.; Yamamoto, T.; Ikuhara, Y. Atomic Structure of [0001]-Tilt Grain Boundaries in ZnO: A High-Resolution TEM Study of Fiber-Textured Thin Films. *Phys. Rev. B* **2004**, *70*, 125415.

(54) Benedek, N. A.; Chua, A. L. S.; Elsässer, C.; Sutton, A. P.; Finnis, M. W. Interatomic Potentials for Strontium Titanate: An Assessment of Their Transferability and Comparison with Density Functional Theory. *Phys. Rev. B* **2008**, *78*, 064110.

(55) Dawson, J. A.; Tanaka, I. Proton Incorporation and Trapping in ZrO₂ Grain Boundaries. *J. Mater. Chem. A* **2014**, *2*, 1400−1408.

(56) Lee, W.-Y.; Bristowe, P. D.; Solorzano, I. G.; Vandersande, J. B. Atomistic Calculations and HRTEM Observations of an [001] Tilt Boundary in Rutile. *Mater. Res. Soc. Symp. Proc.* **1993**, *319*.

(57) Kresse, G.; Furthmuller, J. Efficient Iterative Schemes for Ab Initio Total-Energy Calculations Using a Plane-Wave Basis Set. *Phys. Rev. B* **1996**, *54*, 11169−11186.

(58) Perdew, J.; Burke, K.; Ernzerhof, M. Generalized Gradient Approximation Made Simple. *Phys. Rev. Lett.* **1996**, *77*, 3865−3868.

(59) Stampfl, C.; Ganduglia-Pirovano, M. V.; Reuter, K.; Scheffler, M. Catalysis and Corrosion: The Theoretical Surface-Science Context. *Surf. Sci.* **2002**, *500*, 368−394.

(60) Wei, C.; Yu, L.; Cui, C.; Lin, J.; Wei, C.; Mathews, N.; Huo, F.; Sritharan, T.; Xu, Z. Ultrathin MnO_2 Nanoflakes as Efficient Catalysts for Oxygen Reduction Reaction. *Chem. Commun.* **2014**, *50*, 7885−7888.

(61) Cao, Y. L.; Yang, H. X.; Ai, X. P.; Xiao, L. F. The Mechanism of Oxygen Reduction on MnO_2-Catalyzed Air Cathode in Alkaline Solution. *J. Electroanal. Chem.* **2003**, *557*, 127−134.

17784

dx.doi.org/10.1021/am504351p | *ACS Appl. Mater. Interfaces* 2014, 6, 17776−17784